

Wind regime features and their impacts on the middle reaches of the Yarlung Zangbo River on the Tibetan Plateau, China

ZHANG Yan^{1,2}, ZHANG Zhengcai^{3,4*}, MA Pengfei⁵, PAN Kaijia^{2,3}, ZHA Duo⁶, CHEN Dingmei⁶, SHEN Caisheng⁷, LIANG Aimin⁴

¹ Institute of Atmosphere Physics, Chinese Academy of Sciences, Beijing 100029, China;

² University of Chinese Academy of Sciences, Beijing 100083, China;

³ Key Laboratory of Desert and Desertification, Northwest Institute of Eco-environment and Resources, Chinese Academy of Sciences, Lanzhou 730000, China;

⁴ Shaanxi Normal University, Xi'an 710119, China;

⁵ Tibet Climate Center, Lhasa 850000, China;

⁶ Shannan Meteorological Bureau, Shannan 856000, China;

⁷ Policy Research Office of Party Committee of Tibet Autonomous Region, Lhasa 850000, China

Abstract: The wide valley of the Yarlung Zangbo River is one of the most intense areas in terms of aeolian activity on the Tibetan Plateau, China. In the past, the evaluation of the intensity of aeolian activity in the Quxu–Sangri section of the Yarlung Zangbo River Valley was mainly based on data from the old meteorological stations, especially in non-sandy areas. In 2020, six new meteorological stations, which are closest to the new meteorological stations, were built in the wind erosion source regions (i.e., sandy areas) in the Quxu–Sangri section. In this study, based on mathematical statistics and empirical orthogonal function (EOF) decomposition analysis, we compared the difference of the wind regime between new meteorological stations and old meteorological stations from December 2020 to November 2021, and discussed the reasons for the discrepancy. The results showed that sandy and non-sandy areas differed significantly regarding the mean velocity (8.3 (± 0.3) versus 7.7 (± 0.3) m/s, respectively), frequency (12.9% ($\pm 6.2\%$) versus 2.9% ($\pm 1.9\%$), respectively), and dominant direction (nearly east or west versus nearly north or south, respectively) of sand-driving winds, drift potential (168.1 (± 77.3) versus 24.0 (± 17.9) VU (where VU is the vector unit), respectively), resultant drift potential (92.3 (± 78.5) versus 8.7 (± 9.2) VU, respectively), and resultant drift direction (nearly westward or eastward versus nearly southward or northward, respectively). This indicated an obvious spatial variation in the wind regime between sandy and non-sandy areas and suggested that there exist problems when using wind velocity data from non-sandy areas to evaluate the wind regime in sandy areas. The wind regime between sandy and non-sandy areas differed due to the differences in topography, heat flows, and their coupling with underlying surface, thereby affecting the local atmospheric circulation. Affected by large-scale circulations (westerly jet and Indian monsoon systems), both sandy and non-sandy areas showed similar seasonal variations in their respective wind regime. These findings provide a credible reference for re-understanding the wind regime and scientific wind-sand control in the middle reaches of the Yarlung Zangbo River Valley.

Keywords: wind regime; aeolian activity; sand-driving winds; drift potential; atmospheric circulation; Yarlung Zangbo River; Tibetan Plateau

Citation: ZHANG Yan, ZHANG Zhengcai, MA Pengfei, PAN Kaijia, ZHA Duo, CHEN Dingmei, SHEN Caisheng, LIANG Aimin. 2023. Wind regime features and their impacts on the middle reaches of the Yarlung Zangbo River on the Tibetan Plateau, China. *Journal of Arid Land*, 15(10): 1174–1195. <https://doi.org/10.1007/s40333-023-0066-8>

*Corresponding author: ZHANG Zhengcai (E-mail: zhangzhengcai@snnu.edu.cn)

Received 2023-04-06; revised 2023-06-23; accepted 2023-07-04

© Xinjiang Institute of Ecology and Geography, Chinese Academy of Sciences, Science Press and Springer-Verlag GmbH Germany, part of Springer Nature 2023

1 Introduction

Aeolian activity is a common natural phenomenon in arid and semi-arid areas, which can pose a serious challenge to local ecosystems, economic development, air quality and human health (Hefflin et al., 1994; Huang et al., 2016; Dong et al., 2017; Li et al., 2021a). It is the main driving force of surface sediment migration and aeolian landform evolution, and is responsible for sand-dust storms, aeolian hazards and land desertification in arid and semi-arid areas (Bagnold, 1941; Fryberger and Dean, 1979; Pye and Tsoar, 2009; Dong et al., 2017). Aeolian activity causes the movement of sand particles along with the airflow (Shao, 2008; Kok et al., 2012). Strong winds are the driving force of this phenomenon and the fundamental meteorological factor in aeolian research.

Research on the spatial and temporal features of the wind regime and their impacts is key to understanding the characteristics of aeolian activity and is also the basis for understanding land desertification combined with sand-dust weather forecasting and forewarning. Previous studies have drawn attention to several key features of the wind regime in aeolian research (Ma et al., 2021c). First, the transit of meso-scale cyclones or anticyclones is often accompanied by strong winds, which are a prerequisite for sand-dust weather (Wang et al., 2017; Zhang et al., 2019; Yang et al., 2022; Zhao et al., 2022). Second, in alpine and valley areas, wind velocity is often weakened by topographic barriers (Ngo and Letchford, 2009). However, when the wind direction is close to a river valley alignment, wind velocity tends to increase because of the funneling effect of the terrain (Zhou et al., 2019), thereby increasing the risk of wind erosion on the surface. Third, in the case of large relative elevation differences, uneven surfaces and diurnal changes in the thermal balance can stimulate local atmospheric circulation, such as mountain-valley winds, which can affect the transport and diffusion paths of fine particles (Baumbach and Vogt, 1999; Shrestha et al., 2016; Bei et al., 2018). Fourth, near-surface wind velocity is affected by the stability of the atmospheric boundary layer (Stout, 2015; He et al., 2022). When the atmosphere is unstable, momentum from the higher layer is transmitted downward, and then surface wind velocity increases; strong vertical mixing increases the intensity of the wind-draft sand flow (Lü and Dong, 2008).

Compared to research conducted on low-altitude valleys and plains (Walker et al., 1987; Dong et al., 2013; Zhang et al., 2014, 2015; Gao et al., 2019; Liu et al., 2019b; Meng et al., 2022), few studies have been done on the wind regime related to aeolian activity in plateau mountain-valley areas. Under such topographic conditions, the wind regime is not only affected by atmospheric circulation but also by local circulation that is stimulated by dynamic local-scale heat flow. This phenomenon occurs widely on the Tibetan Plateau of China where high mountains, shifting sandy land, vegetated land and river surfaces coexist. The Quxu–Sangri section of the Yarlung Zangbo River Valley on the Tibetan Plateau, a typical wide valley, is relatively well populated; however, aeolian activity is frequent owing to the large quantities of unconsolidated sediments as well as windy and dry climate (Dong et al., 2017). Aeolian activity in this wide valley has exacerbated the fragility of local ecosystems, leading to decreased air quality and land fertility, and even affecting transportation (e.g., construction of underground highways) and resident health (Li et al., 2010). However, research on aeolian activity in this region has not been sufficiently studied, especially regarding the driving force (wind regime) for the occurrence of aeolian activity.

Presently, aeolian research in the Quxu–Sangri section has focused on the following four topics. (1) Inter-annual and seasonal variations in wind velocity. Studies have shown that wind velocity in this region decreased gradually from the 1980s to the early 2010s but increased gradually thereafter (Liu et al., 2019a; Ben et al., 2020; Yang et al., 2020; Ma et al., 2021b). Wind velocity was higher in winter and spring than in summer and autumn. (2) Inter-annual and seasonal variations in the number of days with winds, dust, and sandstorms. Zhang et al. (2018) counted the number of days with evident aeolian sand transport from 1981 to 2016 based on data from two stations in the Quxu–Sangri section; they found that the number of days with strong winds and sandstorms decreased significantly ($P < 0.001$) whereas the number of days with floating dust increased significantly ($P < 0.05$), and the number of days with strong winds and

sandstorms was greater in winter and spring than in summer and autumn. (3) Spatial and temporal characteristics of drift potential (DP) and aeolian sediment transport rate. Yang et al. (2020) used wind velocity data from one station of the Quxu–Sangri section to calculate DP based on the method of Fryberger and Dean (1979) and revealed that DP was greater in winter and spring than in summer and autumn. Ma et al. (2021b) reached similar conclusions based on wind velocity data from five different stations in this region and found that DP varied among these stations. Zhang et al. (2022a) used the Big Spring Number Eight sampler to collect aeolian sediments and suggested that the sand transport rate was highest in winter and spring, indicating strong aeolian activity during these seasons. (4) Effects of wind erosion on soil grain size composition and nutrient content. Li et al. (2012) studied the grain size distribution and nutrient status of soil at different depths in different land surface types and pointed out that aeolian activity had an important impact on the migration and loss of fine soil particles and the redistribution of soil nutrients. Ma et al. (2021a) reached a similar conclusion by analyzing soil samples from different parts of the landscape.

The findings of the abovementioned studies not only provide valuable information about the features of the wind regime and its effects on the surface sediments in the Yarlung Zangbo River Valley, but also support efforts to prevent aeolian hazards and control land desertification. However, there are still several problems with the available data. First, the temporal resolution of the analyzed data is low, making it difficult to fully describe the features of the wind regime in the region. Second, the Quxu–Sangri section belongs to a complex river–mountain system with a complicated near-surface wind field, and the meteorological stations from which data were analyzed in the previous research are few and far away from sandy areas; therefore, they cannot truly reflect the features of the wind regime in sandy areas (especially for wind direction). Third, the causes of the spatial and temporal differences in the wind regime were not identified. For these reasons, more studies, especially on the wind regime changes in relation to geomorphology, need to be conducted.

From this perspective, in this study, we used wind velocity datasets from six new meteorological stations built in September 2020 in sandy areas (river mudflats and piedmont shifting sandy land) of the Quxu–Sangri section, and from six old meteorological stations located in non-sandy areas (gully grasslands and gravel-covered land) close to the new meteorological stations (i.e., within 6.2–12.5 km of each other; Table 1), to analyze the features of the local wind regime. This study will expand the data available to aeolian research and assist the prevention and control of aeolian hazards near the Yarlung Zangbo River. More importantly, the results can provide insights into the formation and development of aeolian activity in mountain-valley terrain and strengthen our comprehension of aeolian activity processes in high-elevation arid and semi-arid areas.

2 Study area

The study area is the Quxu–Sangri section (29°10′–29°30′N, 90°40′–92°10′E) of the Yarlung Zangbo River Valley, which lies in the southern part of the Tibetan Plateau, China, with elevations ranging from 3550 to 3600 m a.s.l. (decreasing from west to east) in the main stream valley (Fig. 1). Bordered by the Nyaiqentanglha Mountains to the north and the Himalayas to the south, it presents a complex river–mountain system characterized by complicated topography. The region is mainly located in temperate and semi-arid climate zone. The annual average temperature is about 8.7°C, with monthly average temperature ranging from −1.2°C (in January) to 16.8°C (in August) (Zhang et al., 2022b). The annual precipitation is about 378 mm with a single-peaked curve of monthly variation, and most of annual precipitation (>60%) occurs during the rainy season, from May to August (Zhang et al., 2022b). At the spatial scale, precipitation gradually increases from west to east. The annual average relative humidity is 42% and tends to increase from west to east, being wetter in summer and drier in winter. Aeolian sediments are widely distributed in this region, which together with fluvial sediments form the source of current aeolian activity (Ling et al., 2021;

Ma et al., 2021c; Zhang et al., 2021). In recent years, aeolian activity shows an increasing frequency in the study area, which occurs mainly from December to May of the following year and is controlled by the strength and location of the westerly jet (Ling et al., 2019).

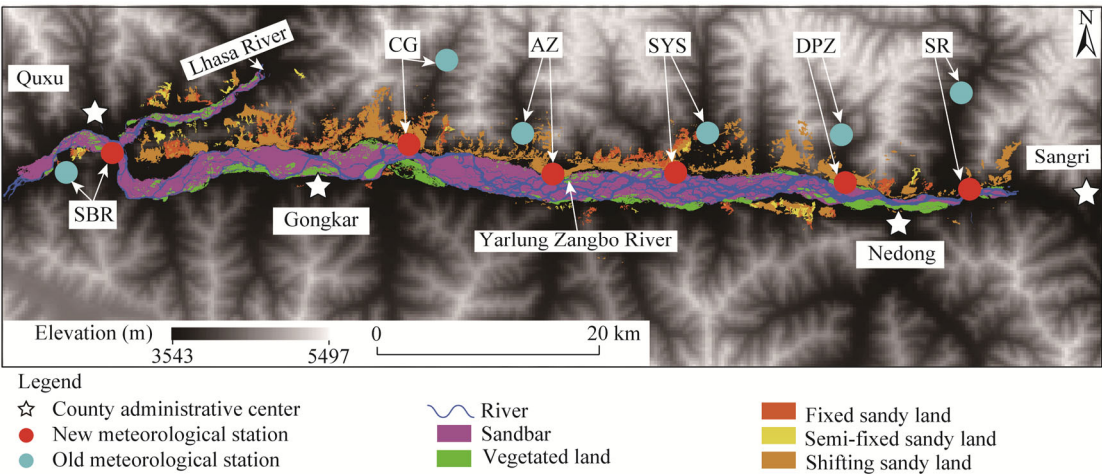


Fig. 1 Overview of the Quxu–Sangri section of the Yarlung Zangbo River Valley and spatial distribution of new meteorological stations in sandy areas and old meteorological stations in non-sandy areas. SBR, CG, AZ, SYS, DPZ and SR represent the six sites, with each having a pair of new meteorological station and old meteorological station. The elevation data were downloaded from the website of <https://search.asf.alaska.edu/>, and land use type data were obtained from Ma et al. (2021b).

3 Data sources and methods

3.1 Data sources

In this study, we focused on the velocity and direction of sand-driving winds (i.e., winds with a velocity greater than 6.5 m/s), as aeolian activity is mainly controlled by these winds. Wind velocity datasets from six new meteorological stations and six old meteorological stations in both sandy and non-sandy areas were provided by the Shannan Meteorological Bureau, including free-stream wind velocity and direction at 10 m above the ground for a complete year (from 1 December 2020 to 30 November 2021) (Fig. 1; Table 1). Ultrasonic wind sensors (WXT520,

Table 1 Ambient conditions of all new meteorological stations and old meteorological stations at the six sites

Site	Station	Ambient condition
SBR	NMS	Main-stream river valley; semi-fixed sandy land
	OMS	Tributary valley; grassland; 8.26 km from NMS
CG	NMS	Main-stream river valley; shifting sandy land
	OMS	Tributary valley; grassland; 10.90 km from NMS
AZ	NMS	Main-stream river valley; shifting sandy land
	OMS	Tributary valley; grassland and cultivated land; 6.21 km from NMS
SYS	NMS	Main-stream river valley; shifting sandy land
	OMS	Tributary valley; grassland and construction land for road; 6.32 km from NMS
DPZ	NMS	Main-stream river valley; shifting sandy land
	OMS	Tributary valley; grassland and building land; 6.32 km from NMS
SR	NMS	Main-stream river valley; shifting sandy land
	OMS	Tributary valley; grassland and woodland; 12.50 km from NMS

Note: SBR, CG, AZ, SYS, DPZ and SR represent the six sites, with each having a pair of old meteorological station (OMS) and new meteorological station (NMS). The types of land use near the OMS were obtained from field observations.

Vaisala, Helsinki, Finland) were utilized to measure wind velocity and direction. Data were recorded continuously and stored as 1-h mean values with a resolution of 0.1 m/s and 1° for wind velocity and direction, respectively.

3.2 Spatial and temporal decomposition of wind velocity

Empirical orthogonal function (EOF) decomposition allows for the separation of temporal and spatial variations in the element field. It also contributes to the characterization of the main spatial and temporal structures of the element field with as few modes as possible (Wei, 2007). The decomposition process of wind velocity in R software is as follows.

(1) Generating the wind velocity matrix $X_{n \times m}$.

$$X_{n \times m} = \begin{bmatrix} u_{11} & \cdots & u_{1m} \\ \cdots & \cdots & \cdots \\ u_{n1} & \cdots & u_{nm} \end{bmatrix}, \quad (1)$$

where, $X_{n \times m}$ is a matrix of wind velocity data; and u_{nm} is the value of wind velocity (m/s), in which n is the number of observations and m is the number of meteorological stations.

(2) Determining the correlation coefficient matrix, eigenvalue matrix and eigenvector matrix for $X_{n \times m}$.

$$C_{m \times m} = \text{Cor}(X_{n \times m}), \quad (2)$$

$$A_{1 \times m} = \text{Eigen}(C_{m \times m}), \quad (3)$$

$$V_{m \times m} = \text{Eigen}(C_{m \times m}), \quad (4)$$

where, $C_{m \times m}$ is a correlation coefficient matrix of $X_{n \times m}$; $\text{Cor}(X_{n \times m})$ is a function used in the R software to calculate the correlation coefficient matrix; $A_{1 \times m}$ is the eigenvalue matrix of $C_{m \times m}$; $\text{Eigen}(C_{m \times m})$ is a function used in the R software to calculate the eigenvalue matrix and eigenvector matrix; and $V_{m \times m}$ is the eigenvector matrix of $C_{m \times m}$. Each eigenvector corresponds to a spatial mode. According to the theory of EOF, there will be m modes that are equal to the number of meteorological stations. The first, second, and m^{th} mode are defined on the basis of the magnitude of the eigenvalue, so the first mode has the largest eigenvalue.

(3) Calculating the time coefficient matrix.

$$T_{n \times m} = X_{n \times m} V_{m \times m} = \begin{bmatrix} t_{11} & \cdots & t_{1m} \\ \cdots & \cdots & \cdots \\ t_{n1} & \cdots & t_{nm} \end{bmatrix}, \quad (5)$$

where, $T_{n \times m}$ is the matrix of time coefficient; and t_{nm} is the time coefficient.

(4) Obtaining the cumulative variance contribution.

$$\text{CVC}_p = \left(\sum_{i=1}^{i=p} \lambda_i / \sum_{i=1}^{i=m} \lambda_i \right) \times 100\%, \quad (6)$$

where, CVC_p (%) is the cumulative variance contribution of the first p eigenvector ($p \leq m$); and λ_i is the i^{th} eigenvalue. Accordingly, we selected those spatial modes with a total CVC_p of greater than 80%, i.e., when $p=3$, CVC_3 is greater than 80%.

In addition, to highlight the temporal variation of the modes in this study, we considered the time coefficient anomaly series for each mode:

$$\text{TCA} = t_{j,j} - \overline{t_{j,j}}, \quad (7)$$

where, TCA is the time coefficient anomaly; $t_{j,j}$ denotes the temporal coefficient series of the j^{th} mode (i.e., the j^{th} column of $T_{n \times m}$); and $\overline{t_{j,j}}$ is the arithmetic mean. Time coefficient anomaly fluctuates around zero; values greater than zero indicating that the mode is strengthening at that time, while values less than zero indicating that the mode is weakening.

3.3 Dominant wind direction

Wind direction determines the path of aeolian sediment transport and is therefore considered as an important factor in aeolian research (Zhang et al., 2015). Previous studies have shown that the

regional wind direction distribution is complex (e.g., Liu et al., 2019a). To quantify the wind direction distribution in the study area, we used a common method from aeolian geomorphology research fields, i.e., Gaussian mode (Lü et al., 2014). Wind direction generally has a multi-peaked distribution, and a single Gaussian mode cannot completely describe the overall wind direction distribution. Thus, a mixed Gaussian mode was typically used to represent the wind direction distribution:

$$P_k(\theta) = \sum_{k=1}^{k=n_\theta} \frac{w_k}{\sigma_k} \exp \left[-\frac{(\theta - \theta_k)^2}{2\sigma_k^2} \right], \quad (8)$$

where $P_k(\theta)$ indicates the probability density of wind direction θ ($^\circ$; clockwise from due north); n_θ is the number of Gaussian mode functions; w_k and σ_k ($^\circ$) denote the weight and standard deviation of the k^{th} dominant wind direction, respectively; and θ_k ($^\circ$) is the k^{th} dominant wind direction. It should be noted that $\sum w_k$ is equal to 1. We used the expectation maximization algorithm to estimate the parameters for the annual and quarterly dominant wind directions based on the mixtools package in R software (Benaglia et al., 2009).

In addition, the following two equations were used to calculate the average wind velocity and frequency of sand-driving winds:

$$\overline{u_{sdw}} = \sum_{i=1}^{i=N} u_i / N, \quad (9)$$

$$F_{sdw} = N / S, \quad (10)$$

where, $\overline{u_{sdw}}$ (m/s) is the average wind velocity of sand-driving winds; N (d) is the number of days with sand-driving winds; u_i (m/s) is the wind velocity of the i^{th} sand-driving wind; F_{sdw} is the frequency of sand-driving winds; and S is the number of wind data.

3.4 DP calculation

DP (VU) indicates the ability of the airflow to transport sand over a period of time and is therefore used as an important indicator reflecting the intensity of aeolian activity. We calculated the DP as follows (Fryberger and Dean, 1979):

$$DP = u^2(u - u_c)f, \quad (11)$$

$$DP_E = \sum DP \sin(\alpha), \quad (12)$$

$$DP_N = \sum DP \cos(\alpha), \quad (13)$$

$$RDP = \sqrt{DP_E^2 + DP_N^2}, \quad (14)$$

$$RDD = \tan^{-1}(DP_E / DP_N), \quad (15)$$

where, DP (VU) is the drift potential; u (knots) and u_c (knots) represent the wind velocity and critical wind velocity for sand driving recorded at a height of 10 m above the ground surface ($u \geq u_c$), respectively; f is the frequency of wind velocity u ; DP_E (VU) is the component of DP in the east-west direction; DP_N (VU) is the component of DP in the north-south direction; α ($^\circ$; clockwise from due north) is the direction in which the wind is blowing; RDP (VU) is the resultant drift potential; and RDD ($^\circ$) is the resultant drift direction. The equation for calculating the critical wind velocity u_c is as follows (Bagnold, 1941):

$$u_c = 5.75A\sqrt{gd(\rho_p - \rho_a / \rho_a)} \log(z / z_0), \quad (16)$$

where, A is an empirical coefficient (with a value of 0.1); g is the acceleration due to gravity (9.8 m/s^2); d (m) is the sand grain size, taken as $2.0 \times 10^{-4} \text{ m}$ (Zhang et al., 2021); ρ_p is the sand particle density (2650.00 kg/m^3 ; Kok et al., 2012); ρ_a is the air density (0.82 kg/m^3) calculated by the equation of the state of ideal gas; z (m) denotes the height above the ground surface (10 m height); and z_0 (m) denotes the aerodynamic roughness length, which is taken as $3.4 \times 10^{-4} \text{ m}$ (Zhang et al., 2022a). Then, the calculated u_c value for the study area is 6.5 m/s.

4 Results

4.1 Spatial mode characteristics of regional wind velocity

There were three main spatial modes of monthly average wind velocity in the study area (Table 2). Mode I reflects the homogeneity of regional wind velocity, whereas Mode II and Mode III reflect the regional heterogeneity of wind velocity. The cumulative variance contribution of Mode I was 49% and eigenvalues for all eigenvectors were positive (ranging from 0.18 to 0.33; Table 2). The cumulative variance contribution of Mode II was 21%, with eigenvalues positive in sandy areas (ranging from 0.12 to 0.39) and negative in non-sandy areas (ranging from -0.34 to -0.23), except for the non-sandy area at the SBR site. The cumulative variance contribution of Mode III was 11%, with eigenvalues negative in the western part of the study area (SBR, CG and AZ) and positive in the eastern part (SYS, DPZ and SR). The cumulative variance contributions of these three main spatial modes together accounted for more than 80% of the total spatial distribution information of regional wind velocity.

Table 2 Spatial modes and eigenvalues of their eigenvectors for regional wind velocity at the six sites in sandy and non-sandy areas

Spatial mode	CVC (%)	Eigenvalue											
		SBR		CG		AZ		SYS		DPZ		SR	
		SA	NSA	SA	NSA	SA	NSA	SA	NSA	SA	NSA	SA	NSA
Mode I	49	0.28	0.30	0.29	0.29	0.30	0.28	0.36	0.33	0.24	0.28	0.18	0.30
Mode II	21	0.12	0.17	0.29	-0.34	0.39	-0.32	0.19	-0.23	0.33	-0.34	0.29	-0.34
Mode III	11	-0.47	-0.27	-0.34	-0.12	-0.11	0.10	0.05	0.03	0.46	0.26	0.53	0.06

Note: CVC, cumulative variance contribution; SA, sandy area; NSA, non-sandy area.

The three spatial modes of wind velocity had strong or weak forms, depending on the seasons (Fig. 2). The time coefficient anomaly of Mode I was close to 0.00 in winter (December, January and February; ranging from -0.05 to -0.01), significantly greater than 0.00 from March to July (ranging from 0.61 to 2.41) and significantly less than 0.00 from August to November (ranging from -1.49 to -0.16) (Fig. 2a). There was a weakening trend of the time coefficient anomaly from April to September, and a strengthening trend from September to November. The time coefficient anomaly of Mode II was positive from April to September (ranging from 0.21 to 1.35) and negative in other months of the year (ranging from -0.74 to -0.11), with a strengthening trend from March to July and a weakening trend from July to March of the following year (Fig. 2b). The time coefficient anomaly of Mode III was positive in February, March, October and November (ranging from 0.20 to 0.68), and negative in the other months of the year (ranging from -0.02 to -0.52) (Fig. 2c).

4.2 Velocity and frequency of sand-driving winds in sandy and non-sandy areas

Velocity and frequency of sand-driving winds differed significantly between sandy and non-sandy areas (paired *t*-test, $P < 0.05$; Fig. 3). The annual average velocity and frequency of sand-driving winds were respectively 8.3 (± 0.3) m/s and 12.9% ($\pm 6.2\%$) in sandy areas, and 7.7 (± 0.3) m/s and 2.9% ($\pm 1.9\%$) in non-sandy areas; these values in non-sandy areas were 7.3% ($\pm 5.8\%$) and 69.1% ($\pm 31.2\%$) lower than those in sandy areas, respectively. The annual frequency of sand-driving winds increased from west to east in sandy areas but decreased from west to east in non-sandy areas; the difference of the annual frequency of sand-driving winds between the two land cover types increased from west to east, with the smallest difference at the SBR site (0.2%) and the largest differences at the DPZ and SR sites (20.4% and 18.1%, respectively).

The frequency of sand-driving winds in sandy areas was highest in spring (4.3% ($\pm 1.6\%$); Table 3), followed by winter (3.2% ($\pm 1.6\%$)), summer (2.9% ($\pm 1.4\%$)) and autumn (2.4% ($\pm 1.6\%$)). The seasonal variations were similar in non-sandy areas, with the highest wind frequency in spring (1.2% ($\pm 0.8\%$)), followed by winter (0.7% ($\pm 0.4\%$)), summer (0.6% ($\pm 0.7\%$))

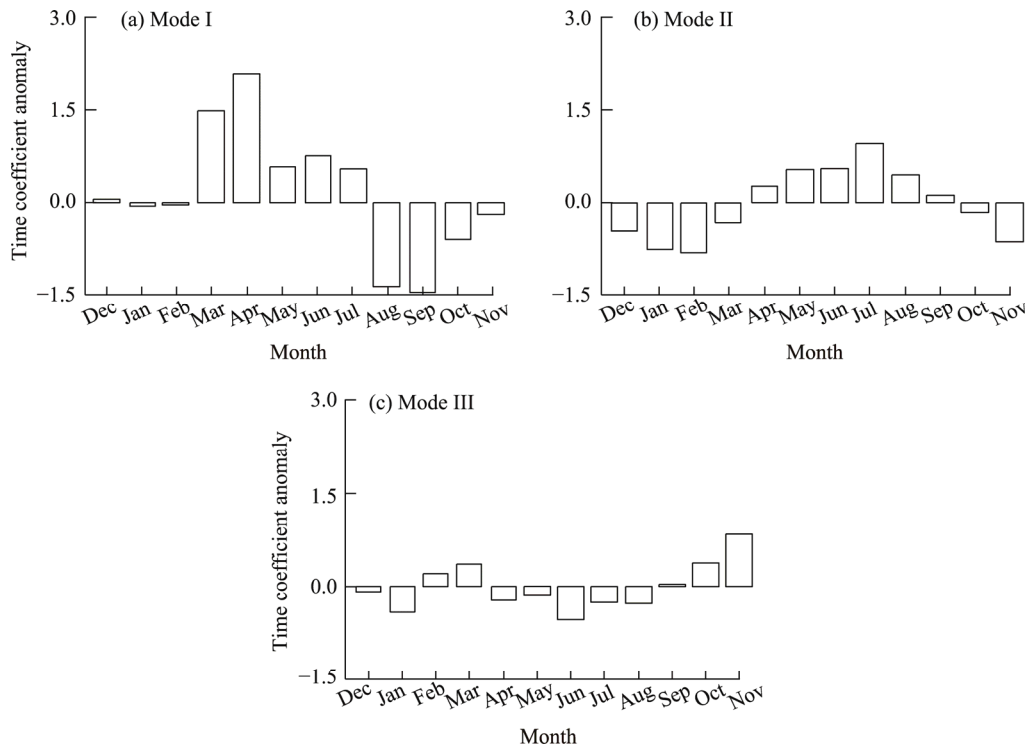


Fig. 2 Time coefficient anomaly of spatial Mode I (a), Mode II (b) and Mode III (c) for wind velocity in the Quxu–Sangri section of the Yarlung Zangbo River Valley from December 2020 to November 2021

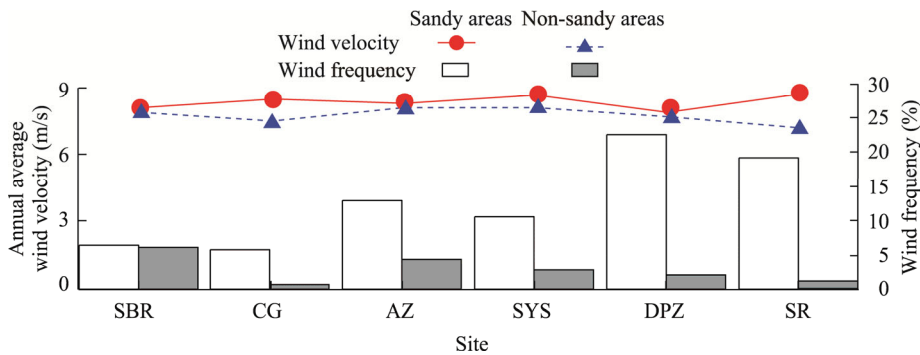


Fig. 3 Comparison of the annual average velocity and frequency of sand-driving winds at the six sites in sandy and non-sandy areas

and autumn (0.3% ($\pm 0.3\%$)). The difference in the frequency of sand-driving winds between sandy and non-sandy areas was higher in spring and summer (30.0% ($\pm 13.2\%$) and 28.9% ($\pm 9.5\%$), respectively), but lower in winter and autumn (22.7% ($\pm 4.5\%$) and 18.4% ($\pm 3.2\%$), respectively).

4.3 Direction of sand-driving winds in sandy and non-sandy areas

Direction of sand-driving winds differed greatly between sandy and non-sandy areas (Fig. 4). The dominant wind direction in sandy areas was generally from east or west. Wind direction at the SBR site showed four peaks, with the dominant wind direction of 274° ($\pm 24^\circ$) ($w=0.48$, where w is the weight of the dominant wind direction). The CG and SYS sites showed three peaks of wind direction, with the dominant wind directions of 268° ($\pm 20^\circ$) ($w=0.51$) and 260° ($\pm 25^\circ$) ($w=0.55$), respectively. There was a bimodal distribution of wind direction at the sites of AZ, DPZ and SR, with the dominant wind directions of 100° ($\pm 20^\circ$) ($w=0.60$), 107° ($\pm 27^\circ$) ($w=0.82$) and 80° ($\pm 15^\circ$) ($w=0.76$), respectively. For non-sandy areas, the annual direction of sand-driving winds at each

Table 3 Comparison of seasonal average wind velocity ($\overline{u_{sdw}}$), wind frequency (F_{sdw}) and dominant wind direction (θ_{sdw}) of sand-driving winds at the six sites in sandy and non-sandy areas

Site	Winter						Spring					
	$\overline{u_{sdw}}$ (m/s)		F_{sdw} (%)		θ_{sdw} (°)		$\overline{u_{sdw}}$ (m/s)		F_{sdw} (%)		θ_{sdw} (°)	
	SA	NSA	SA	NSA	SA	NSA	SA	NSA	SA	NSA	SA	NSA
SBR	7.8	7.6	1.3	1.2	269	258	7.9	8.0	2.8	2.7	284	180
CG	9.1	7.4	1.7	0.3	266	166	8.1	7.2	2.1	0.4	122	175
AZ	9.0	8.3	3.0	1.3	275	149	8.1	7.8	4.7	1.5	100	168
SYS	9.5	8.0	2.8	0.8	261	218	8.3	7.9	3.8	1.1	225	17
DPZ	8.3	7.7	5.7	0.6	110	150	7.7	7.4	7.1	1.0	104	150
SR	8.9	6.9	4.8	0.3	82	200	8.5	7.2	5.3	0.6	78	229

Site	Summer						Autumn					
	$\overline{u_{sdw}}$ (m/s)		F_{sdw} (%)		θ_{sdw} (°)		$\overline{u_{sdw}}$ (m/s)		F_{sdw} (%)		θ_{sdw} (°)	
	SA	NSA	SA	NSA	SA	NSA	SA	NSA	SA	NSA	SA	NSA
SBR	8.4	7.9	1.5	2.1	135	179	7.8	7.4	0.7	0.5	268	89
CG	7.9	8.3	1.2	0.1	120	-	8.6	7.9	0.8	0.0	265	-
AZ	7.8	7.9	3.1	0.9	104	352	8.0	7.8	2.1	0.7	277	158
SYS	8.0	7.8	2.3	0.4	100	18	8.6	8.2	1.6	0.4	257	222
DPZ	7.6	8.0	4.8	0.3	102	23	7.6	7.4	5.0	0.3	108	9
SR	8.5	7.2	4.8	0.1	75	225	8.7	6.7	4.1	0.0	73	-

Note: "-" stands for missing data.

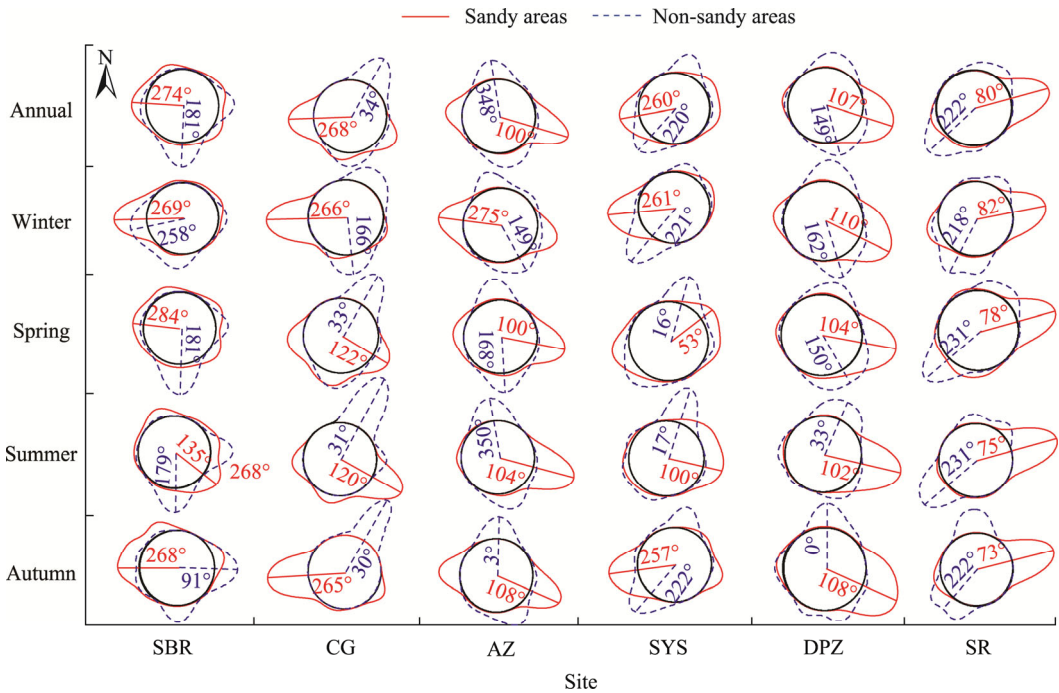


Fig. 4 Seasonal and annual direction distributions of sand-driving winds at the six sites in sandy and non-sandy areas. The distance between the graphed data and the black circle indicates the probability density of wind direction. Values with red and blue fonts indicate the dominant wind direction at new meteorological stations and old meteorological stations, respectively. The red straight lines and the blue dashed lines indicate the position of the dominant wind direction corresponding to the maximum probability density of new meteorological stations and old meteorological stations, respectively.

meteorological station was mainly bimodal, and the dominant wind direction was mainly from south or north: 181° ($\pm 20^{\circ}$), 34° ($\pm 19^{\circ}$), 348° ($\pm 28^{\circ}$), 220° ($\pm 20^{\circ}$), 149° ($\pm 28^{\circ}$) and 222° ($\pm 20^{\circ}$) at the sites of SBR, CG, AZ, SYS, DPZ and SR, respectively. The differences of the dominant wind direction between sandy and non-sandy areas were significant, i.e., 93° , 126° , 112° , 40° , 42° and 142° at the sites of SBR, CG, AZ, SYS, DPZ and SR, respectively.

The dominant direction of sand-driving winds in sandy and non-sandy areas showed large differences among seasons (Table 4). The dominant wind direction in sandy areas exhibited regular seasonal changes; that is, the peaks rose and fell with changing seasons. The proportion of westerly winds (from nearly 270°) decreased gradually from winter to summer, whereas that of easterly winds (nearly 90°) increased gradually. In autumn, wind direction returned to a state similar to that in winter. However, seasonal variations in the dominant direction of sand-driving winds in non-sandy areas were more complex. The data for the secondary and tertiary wind direction are listed in Tables S1 and S2.

Table 4 Dominant direction of sand-driving winds at the six sites in sandy and non-sandy areas

Areas	Site	Winter			Spring			Summer			Autumn		
		w	θ ($^{\circ}$)	σ ($^{\circ}$)	w	θ ($^{\circ}$)	σ ($^{\circ}$)	w	θ ($^{\circ}$)	σ ($^{\circ}$)	w	θ ($^{\circ}$)	σ ($^{\circ}$)
Sandy areas	SBR	0.76	269	23	0.40	284	30	0.45	135	27	0.58	268	38
	CG	0.80	266	20	0.35	122	21	0.61	120	18	0.82	265	17
	AZ	0.61	275	23	0.57	100	18	0.83	104	20	0.59	108	25
	SYS	0.76	261	21	0.48	53	26	0.49	100	23	0.67	257	20
	DPZ	0.79	110	25	0.70	104	30	0.78	102	22	0.45	108	35
	SR	0.67	82	14	0.71	78	15	0.89	75	16	0.82	73	15
Non-sandy areas	SBR	0.54	258	28	0.57	180	20	0.43	179	19	0.5	91	21
	CG	0.53	166	27	0.56	33	21	0.85	36	19	0.95	30	18
	AZ	0.70	149	31	0.56	168	23	0.51	352	25	0.55	3	24
	SYS	0.40	221	22	0.40	16	20	0.54	17	17	0.41	222	20
	DPZ	0.44	162	35	0.61	150	33	0.55	33	26	0.47	0	22
	SR	0.65	218	27	0.65	231	24	0.63	231	20	0.51	222	30

Note: w, weight of the dominant wind direction; θ , dominant wind direction; σ , standard deviation of the dominant wind direction.

4.4 DP in sandy versus non-sandy areas

Annual DP in sandy areas ranged from 60.7 to 322.2 VU (Fig. 5), higher values compared to the results of Yang et al. (2020) (131.0 VU) and Ma et al. (2021b) (5.5 to 77.0 VU). However, annual DP in non-sandy areas ranged from 3.1 to 53.4 VU (Fig. 5), which was 76.5% ($\pm 30.0\%$) lower than that in sandy areas. Annual DP in sandy areas tended to increase from west to east, with the lowest value at the SBR site (60.7 VU) and the highest value at the SR site (322.2 VU). In contrast, annual DP in non-sandy areas tended to decrease from west to east, and the difference of annual DP between sandy and non-sandy areas increased gradually from west to east, with the smallest difference at the SBR site (0.8%) and the largest difference at the SR site (36.9%). Seasonally, DP in sandy areas was highest in winter and spring (37.2% ($\pm 10.5\%$) and 28.3% ($\pm 5.7\%$) of annual DP, respectively) and lowest in summer and autumn (19.1% ($\pm 7.8\%$) and 15.4% ($\pm 3.8\%$) of annual DP, respectively) (Table 5). Seasonal variation of DP in non-sandy areas was similar with that in sandy areas, with the largest proportions in winter and spring (27.0% ($\pm 10.7\%$) and 42.4% ($\pm 13.8\%$) of annual DP, respectively) and the smallest proportions in summer and autumn (21.5% ($\pm 6.4\%$) and 9.1% ($\pm 5.5\%$) of annual DP, respectively). The difference of DP between sandy and non-sandy areas was greatest in winter (40.2% ($\pm 6.7\%$) of annual DP), followed by spring (24.1% ($\pm 3.5\%$) of annual DP), while summer and autumn showed the least significant contributions (17.5% ($\pm 5.3\%$) and 18.2% ($\pm 3.3\%$) of annual DP, respectively).

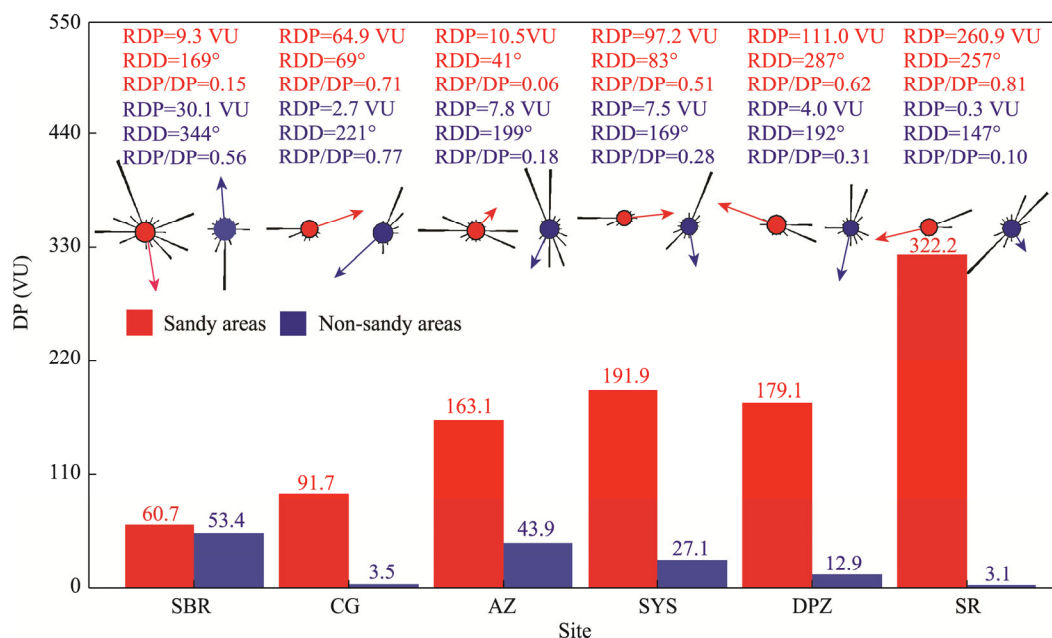


Fig. 5 Comparison of annual sand transport parameters between sandy and non-sandy areas at the six sites. DP, drift potential; RDP, resultant drift potential; RDD, resultant drift direction; RDP/DP, directional variability. Red and blue arrows represent RDD in sandy and non-sandy areas, respectively; red and blue solid circles represent new meteorological stations and old meteorological stations, respectively; the line segments without arrows on the circles represent DP in 16 directions.

Table 5 Comparison of seasonal drift potential (DP), resultant drift potential (RDP) and resultant drift direction (RDD) between sandy and non-sandy areas at the six sites

Site	Winter						Spring					
	DP (VU)		RDP (VU)		RDD (°)		DP (VU)		RDP (VU)		RDD (°)	
	SA	NSA	SA	NSA	SA	NSA	SA	NSA	SA	NSA	SA	NSA
SBR	10.1	6.7	5.9	3.3	97	31	24.4	26.4	2.9	18.2	172	354
CG	43.5	1.4	39.9	0.9	83	225	22.5	1.1	12.5	0.7	33	228
AZ	63.5	16.4	24.7	2.8	88	266	49.6	12.7	11.2	4.2	287	169
SYS	88.5	8.2	73.5	2.1	86	40	48.1	10.7	8.9	7.5	63	198
DPZ	75.8	3.9	43.1	2.4	289	199	45.5	4.6	30.3	1.1	288	257
SR	101.9	0.4	77.9	0.2	255	28	78.5	2.1	57.1	0.3	260	148

Site	Summer						Autumn					
	DP (VU)		RDP (VU)		RDD (°)		DP (VU)		RDP (VU)		RDD (°)	
	SA	NSA	SA	NSA	SA	NSA	SA	NSA	SA	NSA	SA	NSA
SBR	21.0	17.8	7.7	10.1	237	318	5.2	2.4	2.3	1.4	124	294
CG	10.7	0.8	4.4	0.7	3	212	15.1	0.3	14.4	0.3	77	209
AZ	27.4	9.1	19.0	4.0	280	173	22.5	5.6	11.4	1.4	88	311
SYS	24.4	3.4	9.8	2.0	278	177	40.0	4.8	25.0	2.5	87	85
DPZ	28.9	3.0	19.7	1.2	277	162	28.8	1.5	18.2	0.7	293	112
SR	72.4	0.5	66.6	0.1	255	212	69.3	0.1	59.5	0.1	258	172

RDP values in sandy areas ranged from 9.3 to 260.9 VU, which were significantly greater than those in non-sandy areas (ranging from 0.3 to 30.1 VU) (Fig. 5). Directional variability (RDP/DP) indicates the level of concentration of direction of sand drift; the higher the value, the more

concentrated the direction of sand drift. RDP/DP ranged from 0.06 to 0.81 in sandy areas while from 0.10 to 0.77 in non-sandy areas, with the overall trend decreasing from west to east (Fig. 5). RDP/DP values at the SYS, DPZ and SR sites in non-sandy areas were 44.9%, 50.7% and 87.6% lower than those in sandy areas, respectively, whereas the values at the SBR, CG and AZ sites in non-sandy areas were 73.0%, 5.3% and 63.7% lower than those in sandy areas, respectively. In terms of seasons, RDP and RDP/DP differed greatly between sandy and non-sandy areas (Table 5).

The difference in RDD between sandy and non-sandy areas was significant. Annual RDD in sandy areas was generally distributed eastward or westward. At the SBR site, annual RDD in sandy area was 169° (Fig. 5), showing large seasonal differences (RDD rotating clockwise from winter to summer and counterclockwise in autumn) (Table 5). At the CG, AZ and SYS sites, annual RDD values in sandy areas were 69° , 41° and 83° , respectively. There were large seasonal differences among the CG, AZ and SYS sites, but the seasonal variation characteristics of each site were similar (RDD rotating counterclockwise from winter to summer, and then clockwise in autumn). Annual RDD in sandy areas were 287° and 257° at the DPZ and SR sites, respectively, indicating westward sand transport with little seasonal variations. However, the overall annual RDD values in non-sandy areas were southward or northward: 344° at the SBR site, 221° at the CG site, 199° at the AZ site, 169° at the SYS site, 192° at the DPZ site and 147° at the SY site. The difference in annual RDD between non-sandy and sandy areas was largest at the SBR site (175°) and smallest at the SYS site (86°). In conclusion, the features of the wind regime in the study area were both homogeneous and heterogeneous.

5 Discussion

5.1 Influence of atmospheric circulation on the wind regime

Near-surface wind velocity and direction are modulated by the overall atmospheric circulation (Yao et al., 2017). The cumulative variance contribution of Mode I (the dominant spatial pattern of the wind regime in the study area) was 49% (Table 2), indicating the homogeneity of its wind regime. The eigenvectors of Mode I showed positive values for all six sites (Table 2), representing that regional wind velocity was simultaneously increasing or decreasing with spatial consistency. This is mainly because that surface wind regime in the study area is strongly affected by the westerly jet and the Indian monsoon (Yao et al., 2017), and the correlation coefficient (Pearson's r) between surface wind velocity in the study area and the intensity of the westerly jet is as high as 0.70 (Fan et al., 2018). Shan et al. (2019) showed that the Tibetan Plateau was primarily affected by the westerly jet during winter. In spring, the westerly jet weakened rapidly compared to that in winter, and the axis of the westerly jet shifted northward. In summer, the Indian monsoon circulation strengthened, and the westerly jet weakened greatly, with the jet axis moving to 42°N . In autumn, the axis of the westerly jet retreated southward to approximately 34°N , making its central intensity similar to that in spring. In spring and autumn, when the dominant circulation system shifted between the westerly jet and the Indian monsoon, the direction of sand-driving winds in the study area became more complex, with two to four peaks (Fig. 4).

The magnitude of the eigenvalues for eigenvectors in Mode I also reflected the alternating influence of the westerly jet and the Indian monsoon (Table 2). The study area can be divided into three regions from west to east: (1) the SBR–AZ section that is mainly influenced by the westerly jet, had eigenvalues ranging from 0.28 to 0.30; (2) the DPZ–SR section that is mainly influenced by the Indian monsoon, had eigenvalues ranging from 0.18 to 0.30; and (3) the SYS site that is alternately influenced by the two systems, with an eigenvalues from 0.33 to 0.36 in sandy areas.

The time coefficient anomaly values indicated that the values of regional wind velocity under Mode I were generally greater in winter and spring than in summer and autumn (Fig. 2a) and shifted to negative ones in late winter (January to February) and late summer (August). This is consistent with the wind frequency in Table 3, where the frequency of sand-driving winds was 3.2% ($\pm 1.6\%$) and 4.3% ($\pm 1.6\%$) in winter and spring, respectively, versus only 2.9% ($\pm 1.4\%$) and 2.4% ($\pm 1.6\%$) in summer and autumn, respectively. In terms of wind direction, the dominant

direction of sand-driving winds in the SBR–SYS section was between 261° and 275° in winter (with the weight ranging from 0.61 and 0.80), and between 100° and 135° in summer (with the weight ranging from 0.45 to 0.83). However, the annual dominant direction of sand-driving winds in the DPZ–SR section was mainly easterly; that is, it ranged mainly from 73° to 110° (with the weight ranging from 0.45 to 0.89). This finding demonstrated that wind velocity and direction in the study area were being alternately affected by the westerly jet and the Indian monsoon (Shan et al., 2019). In general, the study area is mainly controlled by the westerly jet in winter and the Indian monsoon in summer. In spring, the westerly jet gradually weakens and the study area is affected by the Indian monsoon. From the end of summer (August) to autumn, the Indian monsoon weakens and is gradually replaced by the westerly jet.

5.2 Influence of topography on the wind regime dynamics

The obstructing effect of topography weakens wind velocity and determines the changes in wind direction; however, the funneling effect of topography can increase wind velocity (Chen, 1979). The eigenvectors of Mode II showed positive values in sandy areas while negative values in non-sandy areas (except for the SBR site) (Table 2). This is because the wind regime is influenced by the topography. All meteorological stations in sandy areas are located in the main-stream river valley that is oriented from east to west (Fig. 1a). Their dominant wind direction was 270° ($\pm 45^{\circ}$) in the SBR–SYS section or 90° ($\pm 45^{\circ}$) in the DPZ–SR section, which is close to the orientation of the main-stream river valley. However, the meteorological stations in non-sandy areas are located in tributary valleys with a primarily south-to-north orientation, and the dominant wind direction was 0° ($\pm 45^{\circ}$) or 180° ($\pm 45^{\circ}$), which is close to the orientation of the tributary valleys. The annual average velocity and frequency of sand-driving winds in sandy areas were 7.8–8.6 m/s and 5.8%–22.5%, respectively, which were greater than the corresponding values in non-sandy areas (7.1–8.0 m/s and 0.8%–6.3%, respectively); further, DP in non-sandy areas was 76.5% ($\pm 30.0\%$) lower than that in sandy areas. This showed that topography plays an important role in reducing wind velocity and forcing the change in wind direction.

In addition, the time coefficient anomaly values for Mode II were positive from April to August and negative from September to March of the next year (Fig. 2b), corresponding to seasons dominated by the Indian monsoon and the westerly jet, respectively. This also suggested that wind velocity in the study area is mainly affected by the overall atmospheric circulation pattern, supporting the results of Mode I in the previous section.

For sandy and non-sandy areas, the eigenvalues for eigenvectors in Mode III ranged from -0.47 to -0.11 in the western region (the SBR–AZ section), 0.06 to 0.46 in the eastern region (the DPZ–SR section) and only 0.03 to 0.05 at the SYS site (Table 2). The frequency of sand-driving winds in the DPZ–SR section was from 11.5% to 25.4%, whereas that was only 5.8%–12.9% in the SBR–AZ section. As shown in Figure 3, DP ranged from 179.1 to 322.2 VU in the DPZ–SR section and 60.7 to 163.1 VU in the SBR–AZ section. These values indicated a difference in the wind regime between the eastern and western parts of the study area. In addition, the time coefficient anomaly of Mode III was generally low (negative) in January, June, July and August when the westerly jet or the Indian monsoon was the dominant circulation system, indicating that the difference in the wind regime of the east–west region weakened in these months. Nevertheless, the time coefficient anomaly of Mode III was high (positive) in April, October and November when the dominant wind alternated (Fig. 2c), demonstrating that the difference in the wind regime of the east–west region increased as the dominant circulation system alternated.

The influence of topography on the wind regime is also reflected in the funneling effect. The eastern part of the Quxu–Sangri section of the Yarlung Zangbo River Valley is narrower than the western part, which leads to a stronger funneling effect in the eastern part than in the western part, and wind velocity in the eastern part is generally higher than that in the western part (Li et al., 2010).

5.3 Influence of coupled thermal effects of topography and underlying surface on the wind regime

Thermal flows also play an important role in influencing the wind regime, as heat differences can stimulate local circulation and may cause marked shifts in wind direction over a short-term period (Gevorgyan, 2017). The main surface types in the study area are rivers, sandy lands and grasslands (Shen et al., 2012; Li et al., 2021b). The special topographic features, with high mountains and valleys and an elevation difference of approximately 2000 m between the mountaintops and the river surface in the valleys (Fig. 1a), provide favorable bedforms and topographic conditions for the formation of regional thermal differences. The valley surface types include rivers, woodlands, grasslands and shifting sandy lands (areas with a relatively high thermal capacity), whereas the hillside surface types are mainly grasslands, sandy lands and large area of bare rock (areas with a relatively low thermal capacity) (Luo et al., 2022). Their spatial coupling results in different air temperatures near the hillslope and in the center of the valley at the same elevation, creating a nonhomogeneous horizontal temperature field. A mountain-valley breeze is generated because of these buoyancy effects.

Local currents form on days with weak background circulation changes and on days with clearer, less cloudy weather (Bei et al., 2018). Here, we take the wind direction data in January from sandy areas as an example to discuss the diurnal variation of wind direction (Fig. 6). Data in the other months are provided in Figures S1–S3. The overall diurnal variation in wind direction can be divided into four phases, as shown in Figure 6. Phase I started from 04:00 to 09:00 (Beijing time), when the dominant wind direction was easterly (from 50° to 90°) and relatively concentrated. Phase II, from 10:00 to 13:00, was a period of wind transition when the wind direction rotated clockwise and southerly winds started to increase. Phase III started from 14:00 to 19:00, when the dominant wind direction was westerly (from 230° to 290°). Phase IV was the transition period from 20:00 to 03:00 (the next day), with a clear double peak, a clockwise rotation and a gradual transition from northwesterly (from 314° to 324°) to easterly (from 55° to 89°) winds. The exception was the SBR site, where large difference was found due to the presence of three mountain ranges that lie near the confluence of the Yarlung Zangbo River and the Lhasa River. The wind direction shifted by nearly 180° during the alternation between day and night in sandy areas (Fig. 6a–f), as well as in non-sandy areas with air currents blowing from the valleys to the slopes during the day and from the slopes to the valleys at night (Fig. S2) (Stull, 1988; Gevorgyan, 2017). This indicated obvious mountain-valley wind circulation in the Quxu–Sangri section, with the dominate wind direction of the valley and mountain winds not along the mountain slope but rather following the valley direction. This can be explained by the location of the observation sites on the valley floor.

In addition, the diurnal variation of wind velocity showed a bimodal pattern in sandy areas (hereafter referred to as Pattern I; Figs. 7a and S3), with peaks corresponding to 10:00–11:00 and 17:00–18:00 and troughs corresponding to 08:00 and 13:00. The diurnal variation curves of wind velocity in non-sandy areas showed a single-peaked pattern (hereafter referred to as Pattern II; Figs. 7b and S3), with a peak corresponding to 16:00–17:00 and a trough corresponding to 09:00–10:00. The timing of the shift in wind velocity between sandy and non-sandy areas corresponded to 07:00–09:00 or 08:00–10:00 (sunrise time) in the morning and 19:00–21:00 or 20:00–22:00 (sunset time) in the afternoon. Overall, wind velocity with Pattern I gradually increased after sunrise. This is due to the increased intensity of vertical turbulence in the atmosphere after sunrise and the downward transfer of momentum from the upper layers, both of which increase wind velocity near the ground (Stout, 2015). Wind velocity with Pattern II lagged behind by 1–2 h, probably because of the surface differences, as sand surfaces get warm quickly while grass surfaces get warm slowly. After sunset, wind velocity gradually decreased in both sandy and non-sandy areas. This is because the atmospheric boundary layer tends to stabilize with ground radiation, and the air momentum exchange between the upper and lower layers weakens, resulting in the decrease of wind velocity in the lower layers.

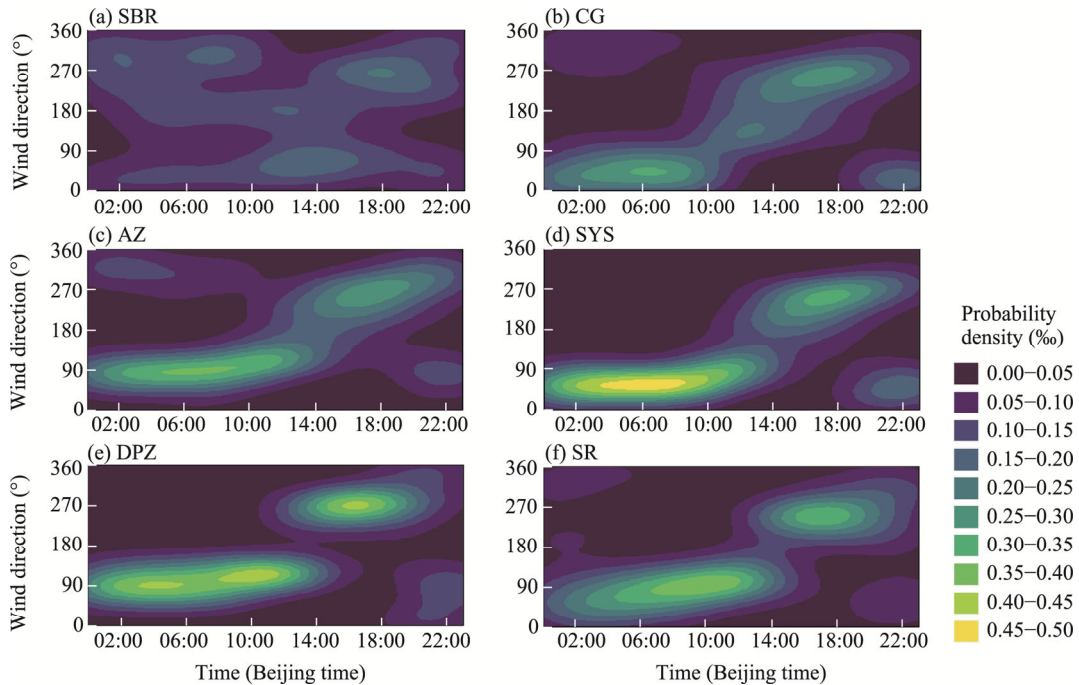


Fig. 6 Diurnal variations of wind direction at the six sites in sandy areas in January. (a), SBR; (b), CG; (c), AZ; (d), SYS; (e), DPZ; (f), SR.

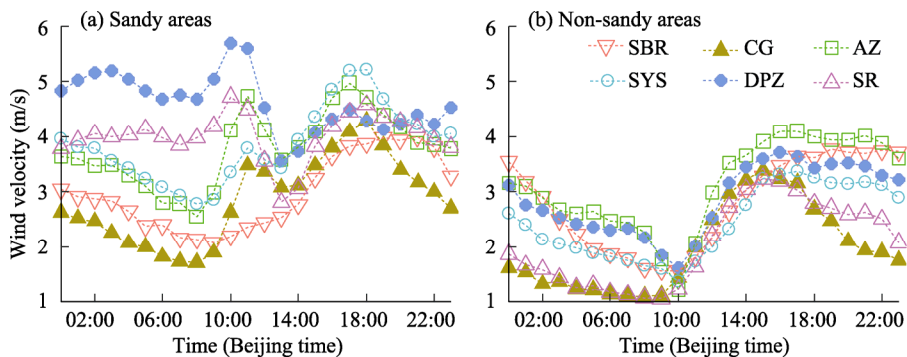


Fig. 7 Diurnal variation curves of wind velocity at the six sites in sandy areas (a) and non-sandy areas (b). Values are means for all months combined.

The reason for the occurrence of trough values in the afternoon under Pattern I may be that the westerly wind prevails in the upper air, and the easterly wind frequency near the ground is high in these regions (Figs. 3 and 4; Table 4). The movement direction of the upper air is opposite to that of the lower air, and the momentum of the upper air is transmitted downward, causing the easterly wind to weaken in the lower layers. This weakening effect is most intense in the afternoon, mainly from 13:00 to 14:00, which leads to the development of a trough in the diurnal variation curve of wind velocity in the afternoon.

6 Conclusions

Frequent and serious aeolian hazards occur in the wide valley of the Yarlung Zangbo River Valley. However, previous studies estimating the intensity of aeolian activity in the Quxu–Sangri section of the Yarlung Zangbo River Valley were based only on wind data from non-sandy areas. In 2020, wind data became available in sandy areas in the Quxu–Sangri section of the Yarlung Zangbo River Valley. So, in this study, we analyzed wind velocity and direction from December 2020 to

November 2021 both in sandy and non-sandy areas of the Quxu–Sangri section in the Yarlung Zangbo River Valley. The main conclusions are as follows:

(1) Conspicuous differences were found in the wind regime between sandy and non-sandy areas. The annual frequency of sand-driving winds, DP and RDP were significantly higher in sandy areas than in non-sandy areas, and the dominant wind direction and RDD in sandy areas also differed greatly from those in non-sandy areas. Stronger wind energy environment in sandy areas may explain why more aeolian activity occurs in sandy areas. Therefore, it is extremely problematic to use wind data from non-sandy areas to evaluate aeolian damage caused by sandy areas under these topographic conditions.

(2) The wind regime was affected by the overall dominant atmospheric circulation, the dynamic and thermal effects of topography and the underlying surface. The atmospheric circulation renders the regional wind regime more homogeneous. When the atmospheric circulation is altered, the wind regime changes systematically throughout the region. However, owing to the differences in topography and underlying surface, different regions respond differently to changes in atmospheric circulation. The blocking effect of topography weakens wind velocity, whereas the funneling effect of topography increases wind velocity, forcing wind direction to adapt to its orientation. In addition, the local circulation generated by the coupling of valley topography and underlying surface is also an important factor affecting the wind regime in different regions.

To accurately forecast dust storms in the Yarlung Zangbo River Valley, it is necessary to construct an observational network that accounts for the topography's influence on the wind regime. In particular, site selection for future meteorological stations should fully consider the local nature of the wind regime (e.g., the difference between nearby sandy and non-sandy areas), and monitoring stations should be established in areas with aeolian activity. Field observations should also be strengthened to take advantage of existing and future stations and attempt to obtain vertical and horizontal profiles for near-surface meteorological indicators, among others. In addition, the harsh natural conditions of the study area bring difficulties to long-term field observations; therefore, researchers should consider developing numerical simulation modes based on empirical data.

Conflict of interest

The authors declare that they have no known competing financial interests or personal relationships that could have appeared to influence the work reported in this paper.

Acknowledgements

This study was supported by the Project for Establishing a Sand-dust Monitoring and Forecast System for the North-bank Settlement Area of the Yarlung Zangbo River (under the 13th Five-year Plan of the Tibet Autonomous Region, China), the Chinese Academy of Sciences Interdisciplinary Innovation Team and the Shannan City Science and Technology Plan Project (E129020301). We thank the editors and anonymous reviewers for their useful suggestions and comments on improving this article.

Author contributions

Conceptualization: ZHANG Zhengcai; Software: ZHANG Yan; Formal analysis and investigation: ZHANG Yan, PAN Kaijia, LIAN Aiming; Writing - original draft preparation: ZHANG Yan; Writing - review and editing: ZHANG Yan, ZHANG Zhengcai; Funding acquisition: ZHANG Zhengcai, MA Pengfei; Resources: MA Pengfei, ZA Duo, CHEN Dingmei, SHEN Caisheng; Supervision: ZHANG Zhengcai.

References

- Bagnold R A. 1941. *The Physics of Blown Sand and Desert Dunes*. London: Methuen, 267–277.
- Baumbach G, Vogt U. 1999. Experimental determination of the effect of mountain-valley breeze circulation on air pollution in the vicinity of Freiburg. *Atmosphere Environment*, 33(24–25): 4019–4027.

- Bei N F, Zhao L N, Wu J R, et al. 2018. Impacts of sea-land and mountain-valley circulations on the air pollution in Beijing-Tianjin-Hebei (BTH): A case study. *Environment Pollution*, 234: 429–438.
- Ben Y, Mei Y D, Chen Y M, et al. 2020. Inter- and intra-annual wind speed variabilities in wide valley regions of the middle reaches of the Yarlung Tsangpo River, China. *Scientific Report*, 10: 12657, doi: 10.1038/s41598-020-69392-2.
- Benaglia T, Chauveau D, Hunter D R, et al. 2009. Mixtools: An R package for analyzing finite mixture models. *Journal of Statistical Software*, 32(6): 1–29.
- Dong Z B, Zhang Z C, Qian G Q, et al. 2013. Geomorphology of star dunes in the southern Kumtagh Desert, China: control factors and formation. *Environmental Earth Sciences*, 69: 267–277.
- Dong Z B, Hu G Y, Qian G Q, et al. 2017. High-altitude aeolian research on the Tibetan Plateau. *Reviews of Geophysics*, 55(4): 864–901.
- Fan W W, Ma W Q, Zheng Y, et al. 2018. Long-term variation of surface heating over the Qinghai-Tibetan Plateau linked to the westerly jet. *Plateau Meteorology*, 37(3): 591–601. (in Chinese)
- Fryberger G S, Dean G. 1979. Dune forms and wind regime. In: McKee E D. *A Study of Global Sand Seas*. Washington: US Government Printing Office, 159–163.
- Gao X M, Dong Z B, Duan Z H, et al. 2019. Wind regime for long-ridge yardangs in the Qaidam Basin, Northwest China. *Journal of Arid Land*, 11(5): 701–712.
- Gevorgyan A. 2017. Summertime wind climate in Yerevan: valley wind systems. *Climate Dynamic*, 48: 1827–1840.
- He P L, Zhang J, Herrmann H J, et al. 2022. Large-eddy simulation of wind-blown sand under unstable atmospheric boundary layer. *Science Bulletin*, 67(14): 1421–1424.
- Hefflin B J, Jalaudin B, McClure E, et al. 1994. Surveillance for dust storms and respiratory diseases in Washington State, 1991. *Archives of Environmental Health*, 49(3): 170–174.
- Huang J P, Yu H P, Guan X D, et al. 2016. Accelerated dryland expansion under climate change. *Nature Climate Change*, 6: 166–174.
- Kok J F, Parteli E J R, Michaels T I, et al. 2012. The physics of wind-blown sand and dust. *Reports on Progress in Physics*, 75(10): 106901, doi: 10.1088/0034-4885/75/10/106901.
- Li C J, Wang Y D, Lei J Q, et al. 2021a. Damage by wind-blown sand and its control measures along the Taklimakan Desert Highway in China. *Journal of Arid land*, 13(1): 98–106.
- Li H D, Shen W S, Zou C X, et al. 2012. Soil nutrients content and grain size fraction of aeolian sandy land in the Shannan Wide Valley of the Yarlung Zangbo River, China. *Acta Ecologica Sinica*, 32(16): 4981–4992. (in Chinese)
- Li P J, Zuo D P, Xu Z X, et al. 2021b. Dynamic changes of land use/cover and landscape pattern in a typical alpine river basin of the Qinghai-Tibet Plateau, China. *Land Degradation and Development*, 32(15): 4327–4339.
- Li S, Yang P, Dong Y X, et al. 2010. *Sandy Desertification and Its Control in Tibet*. Beijing: Science Press, 146–156. (in Chinese)
- Ling Z Y, Jin J H, Wu D, et al. 2019. Aeolian sediments and their paleoenvironmental implication in the Yarlung Zangbo catchment (southern Tibet, China) since MIS3. *Acta Geographica Sinica*, 74(11): 2385–2400. (in Chinese)
- Ling Z Y, Li J S, Jin J H, et al. 2021. Geochemical characteristics and provenance of aeolian sediments in the Yarlung Tsangpo valley, Southern Tibetan Plateau. *Environment Earth Sciences*, 80: 623, doi: 10.1007/s12665-021-09928-5.
- Liu Y, Wang Y S, Shen T. 2019a. Spatial distribution and formation mechanism of aeolian sand in the middle reaches of the Yarlung Zangbo River. *Journal of Mountain Science*, 16(9): 1987–2000.
- Liu Z Y, Dong Z B, Zhang Z C, et al. 2019b. Spatial and temporal variation of the near-surface wind regimes in the Taklimakan Desert, Northwest China. *Theoretical and Applied Climatology*, 138: 433–447.
- Lü P, Dong Z B. 2008. The dependency of sand transport rate by wind on the atmospheric stability: a numerical simulation. *Geomorphology*, 99(1–4): 296–301.
- Lü P, Narteau C, Dong Z B, et al. 2014. Emergence of oblique dunes in a landscape-scale experiment. *Nature Geoscience*, 7: 99–103.
- Luo J, Xin L J, Liu F G, et al. 2022. Study of the intensity and driving factors of land use/cover change in the Yarlung Zangbo River, Nyang Qu River, and Lhasa River region, Qinghai-Tibet Plateau of China. *Journal of Arid Land*, 14(4): 411–425.
- Ma P F, Gao J J, Zha D, et al. 2021a. Analysis of soil nutrients in the aeolian disaster region along middle reaches of Yarlung Zangbo River. *Journal of Arid Land Resources and Environment*, 35(6): 96–101. (in Chinese)
- Ma P F, Lunzhu Q F, Zhang Y, et al. 2021b. Sand supplement characteristics indicated by the area of river inland, flood plain in the riverbed of the Yarlung Zangbo River. *Journal of Desert Research*, 41(3): 25–33. (in Chinese)
- Ma P F, Zhang Z C, Lunzhu Q P, et al. 2021c. Analysis on the sand transport wind power conditions and suggestions on the sand disaster preventions in the middle reaches of Yarlung Zangbo River, China. *Journal of Desert Research*, 41(1): 10–18. (in

Chinese)

- Meng N, Wang N A, Zhao L Q, et al. 2022. Wind regimes and associated sand dune types in the hinterland of the Badain Jaran Desert, China. *Journal of Arid Land*, 14(5): 473–489.
- Ngo T T, Letchford C W. 2009. Experimental study of topographic effects on gust wind speed. *Journal of Wind Engineering and Industrial Aerodynamics*, 97(9–10): 426–438.
- Pye K, Tsoar H. 2009. *Aeolian Sand and Sand Dunes*. London: Unwin Hyman, 56–60.
- Shan X, Zhou S W, Wang M R, et al. 2019. Influence of atmospheric heat anomaly over the Tibetan Plateau on the westerly jet. *Journal of the Meteorological Sciences*, 39(2): 206–213. (in Chinese)
- Shao Y P. 2008. *Physics and Modelling of Wind Erosion*. New York: Springer Science & Business Media, 26–27.
- Shen W S, Li H D, Sun M, et al. 2012. Dynamics of aeolian sandy land in the Yarlung Zangbo River basin of Tibet, China from 1975 to 2008. *Global and Planetary Change*, 86–87: 37–44.
- Stout J E. 2015. Diurnal patterns of blowing dust on the Llano Estacado. *Journal of Arid Environments*, 122: 85–92.
- Stull R B. 1988. *An Introduction to Boundary Layer Meteorology*. Dordrecht: Kluwer Academic Publisher, 26–27.
- Walker A S, Olsen J W, Bagen. 1987. The Badain Jaran desert: remote sensing investigations. *Geographical Journal*, 153(2): 205–210.
- Wang R X, Liu B, Li H R, et al. 2017. Variation of strong dust storm events in Northern China during 1978–2007. *Atmosphere Research*, 183: 166–172.
- Wei F Y. 2007. *Climatological Statistical Diagnosis and Prediction Technology*. Beijing: Meteorological Press, 116–118. (in Chinese)
- Yang J H, Xia D S, Wang S Y, et al. 2020. Near-surface wind environment in the Yarlung Zangbo River basin, southern Tibetan Plateau. *Journal of Arid Land*, 12(6): 917–936.
- Yang X L, Li Y Y, Chen J, et al. 2022. Transmission of rare strong dust and its weather process continuous characteristics in Hexi Corridor. *Arid Land Geography*, 45(5): 1415–1425. (in Chinese)
- Yao T D, Piao S L, Shen M G, et al. 2017. Chained impacts on modern environment of interaction between westerlies and Indian Monsoon on Tibetan Plateau. *Bulletin of Chinese Academy of Sciences*, 32(9): 976–984. (in Chinese)
- Zhang G F, Azorin-Molia C, Shi P J, et al. 2019. Impact of near-surface wind speed variability on wind erosion in the eastern agro-pastoral transitional zone of Northern China, 1982–2016. *Agricultural and Forest Meteorology*, 271: 102–115.
- Zhang H Z, Zhou K S, Duojie S Z, et al. 2018. Analysis of spatiotemporal variation characteristic of wind-sand days in the Yarlung Zangbo River basin during 1981–2016. *Journal of Arid Land Resources and Environment*, 32(12): 131–136. (in Chinese)
- Zhang Y, Ma P F, Zeng L, et al. 2021. Study on silt and clay provenance in the Yarlung Zangbo River middle reaches using sediment physicochemical characteristics. *Journal of Desert Research*, 41(3): 92–100. (in Chinese)
- Zhang Z C, Dong Z B, Wen Q, et al. 2014. Wind regimes and aeolian geomorphology in the western and southwestern Tengger Desert, NW China. *Geological Journal*, 50(6): 707–719.
- Zhang Z C, Dong Z B, Li C X. 2015. Wind regime and sand transport in China's Badain Jaran Desert. *Aeolian Research*, 17: 1–13.
- Zhang Z C, Zhang Y, Ma P F, et al. 2022a. Aerodynamic parameters of typical underlying surfaces in an aeolian region in the middle reaches of the Yarlung Zangbo River. *Arid Zone Research*, 39(04): 997–1005. (in Chinese)
- Zhang Z C, Zhang Y, Ma P F, et al. 2022b. Aeolian sediment transport rates in the middle reaches of the Yarlung Zangbo River, Tibet Plateau. *Science of the Total Environment*, 826: 154238, doi: 10.1016/j.scitotenv.2022.154238.
- Zhao D, Chen S Y, Chen Y. 2022. Comparative analysis of two typical dust storm processes over East Asia. *Journal of Lanzhou University (Natural Science)*, 58(3): 313–322. (in Chinese)
- Zhou C, Yin J Q, Liu Y B. 2019. Effects of wind and rain on the motion of the high-voltage conductor in a simplified valley terrain. *Electric Power Systems Research*, 173: 153–163.

Appendix

Table S1 Dominant wind direction throughout the year and in different seasons in sandy areas

Site	Annual			Winter			Spring			Summer			Autumn		
	w	θ (°)	σ (°)	w	θ (°)	σ (°)	w	θ (°)	σ (°)	w	θ (°)	σ (°)	w	θ (°)	σ (°)
SBR	0.46	274	24	0.76	269	23	0.40	284	30	0.45	135	27	0.58	268	38
	0.35	112	26	0.24	45	22	0.26	124	27	0.31	74	10	0.22	336	16
	0.11	70	17	-	-	-	0.25	63	16	0.16	338	22	0.21	79	21
	0.08	336	20	-	-	-	0.09	336	13	0.09	276	17	-	-	-
CG	0.51	265	25	0.80	266	20	0.35	122	21	0.61	120	18	0.82	265	17
	0.30	121	26	0.11	116	21	0.33	196	23	0.21	266	19	0.13	120	18
	0.19	197	24	0.09	201	24	0.31	264	19	0.18	193	18	-	-	-
AZ	0.60	102	20	0.61	275	23	0.57	100	18	0.83	104	20	0.59	108	25
	0.41	271	18	0.39	102	21	0.43	271	32	0.17	269	16	0.41	277	19
SYS	0.55	265	25	0.76	261	21	0.48	53	18	0.49	100	23	0.67	257	20
	0.24	56	27	0.24	58	22	0.44	225	30	0.29	52	40	0.18	107	17
	0.21	101	28	-	-	-	0.09	91	26	0.23	258	31	0.15	53	24
DPZ	0.82	108	27	0.79	110	25	0.70	104	30	0.78	102	22	0.45	108	35
	0.12	277	15	0.21	277	17	0.27	277	16	0.12	279	14	0.32	275	20
SR	0.76	79	15	0.67	82	14	0.71	78	15	0.89	75	16	0.82	73	15
	0.22	255	22	0.33	255	21	0.29	193	30	-	-	-	0.18	253	24

Note: w, weight of the dominant wind direction; θ , dominant wind direction; σ , standard deviation of the dominant wind direction; -, no data available. SBR, CG, AZ, SYS, DPZ and SR represent the six sites, with each having a pair of old meteorological station and new meteorological station.

Table S2 Dominant wind direction throughout the year and in different seasons in non-sandy areas

Site	Annual			Winter			Spring			Summer			Autumn		
	w	θ (°)	σ (°)	w	θ (°)	σ (°)	w	θ (°)	σ (°)	w	θ (°)	σ (°)	w	θ (°)	σ (°)
SBR	0.45	181	20	0.54	258	28	0.57	180	20	0.43	179	19	0.50	89	21
	0.31	89	28	0.29	188	27	0.25	86	25	0.34	89	20	0.28	179	18
	0.24	255	27	0.18	91	24	0.18	269	23	-	-	-	0.22	273	27
CG	0.56	32	19	0.53	166	27	0.56	33	21	0.85	36	19	1.00	30	18
	0.44	166	25	0.47	37	26	0.44	175	25	0.15	92	15	-	-	-
AZ	0.58	348	28	0.70	149	31	0.56	168	23	0.51	352	25	0.55	2	24
	0.42	156	31	0.30	347	17	0.43	353	24	0.49	158	35	0.45	157	30
SYS	0.43	222	20	0.40	218	22	0.40	17	20	0.54	18	17	0.41	222	20
	0.31	16	16	0.26	20	19	0.37	225	18	-	-	-	0.30	12	24
	-	-	-	-	-	-	0.23	61	20	-	-	-	-	-	-
DPZ	0.51	151	28	0.44	151	35	0.61	150	33	0.55	23	26	0.47	0	22
	0.43	15	31	0.43	12	26	0.34	15	19	0.27	147	27	0.37	165	28
SR	0.64	222	20	0.65	218	27	0.65	229	24	0.63	225	20	0.51	222	35
	0.35	28	32	0.26	28	20	0.35	32	27	0.18	43	18	0.45	358	27

Note: -, no data available.

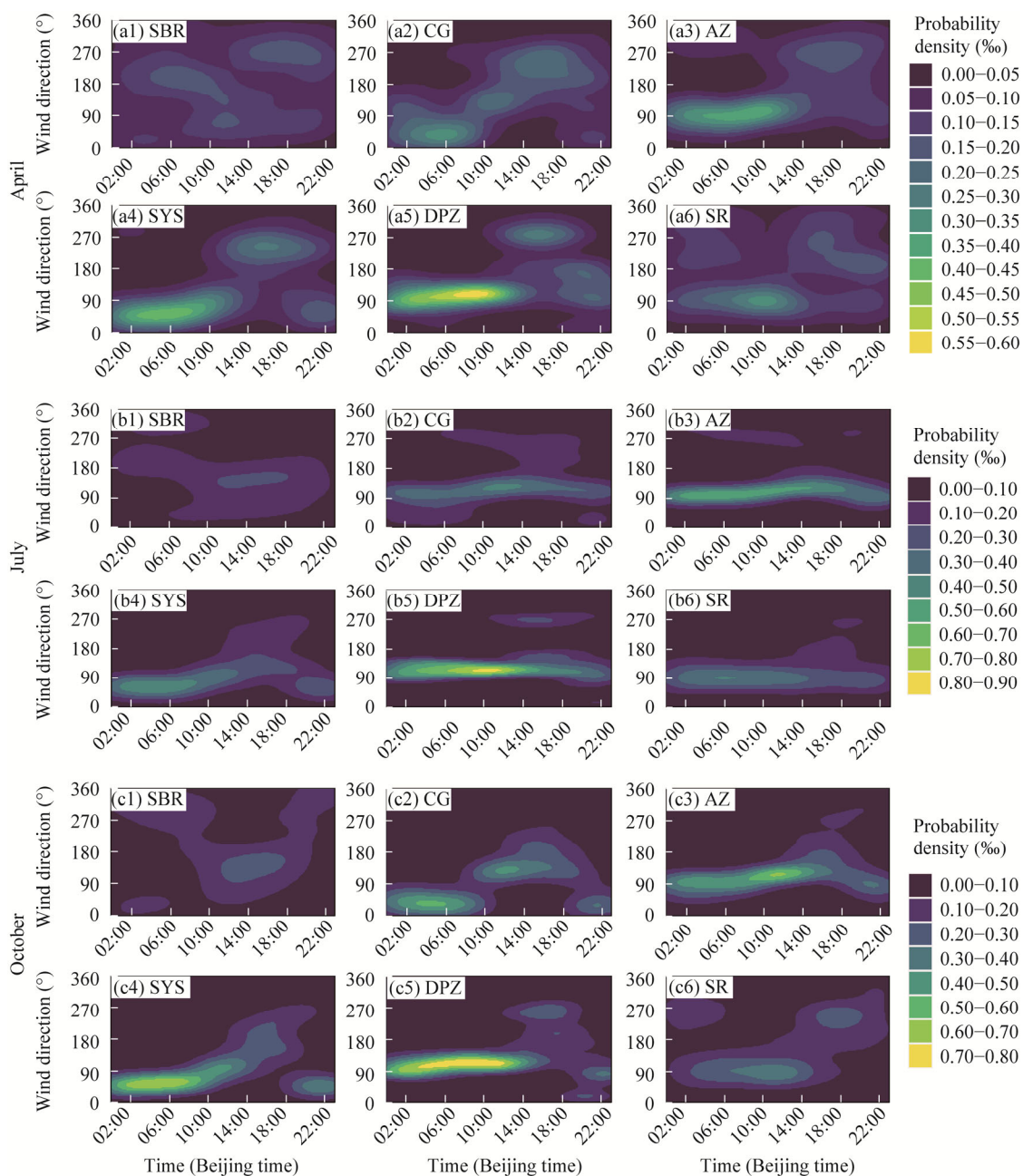


Fig. S1 Diurnal variations of wind direction at the six sites in sandy areas in April (a1–a6), July (b1–b6) and October (c1–c6)

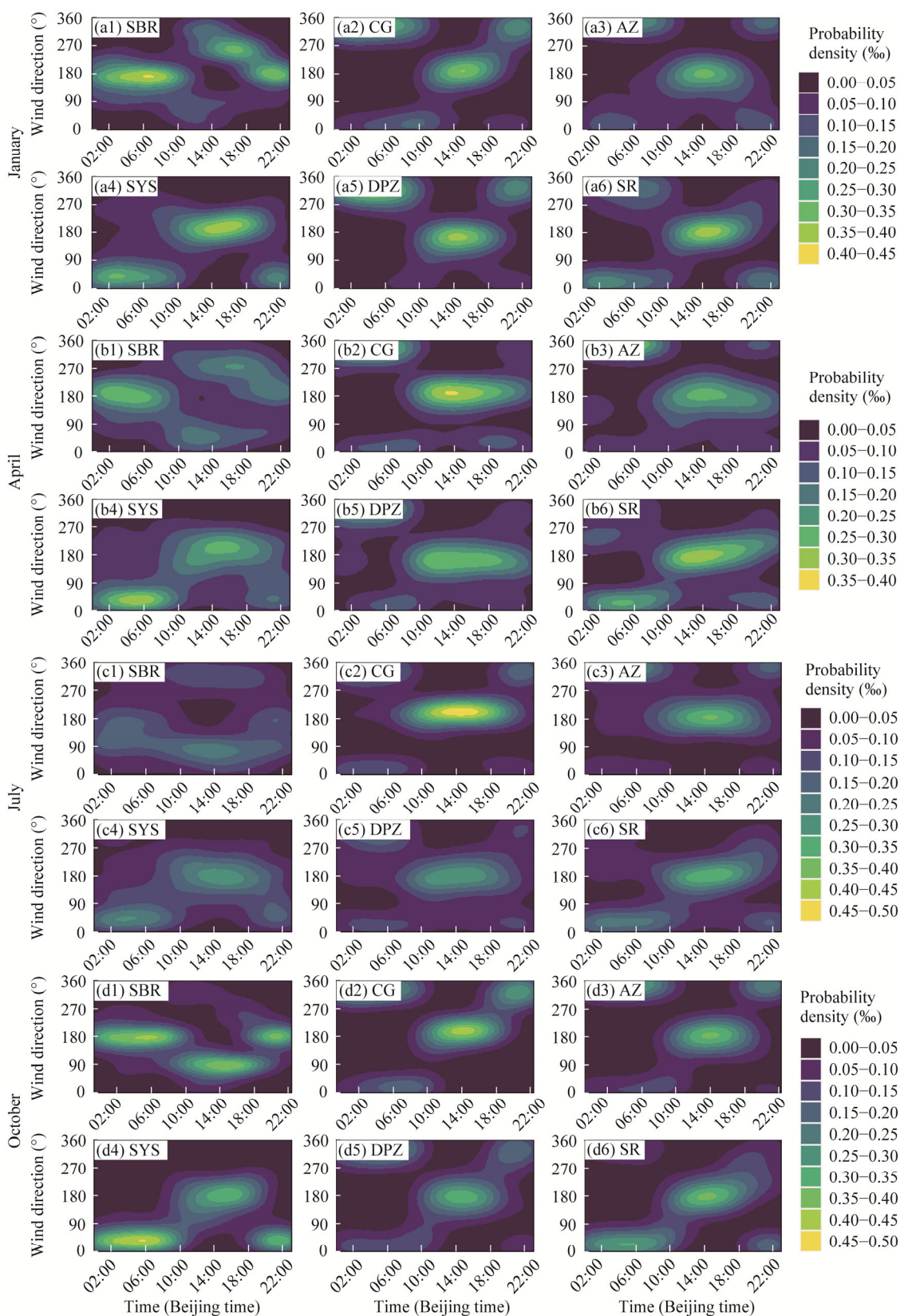


Fig. S2 Diurnal variations of wind direction at the six sites in non-sandy areas in January (a1–a6), April (b1–b6), July (c1–c6) and October (d1–d6)

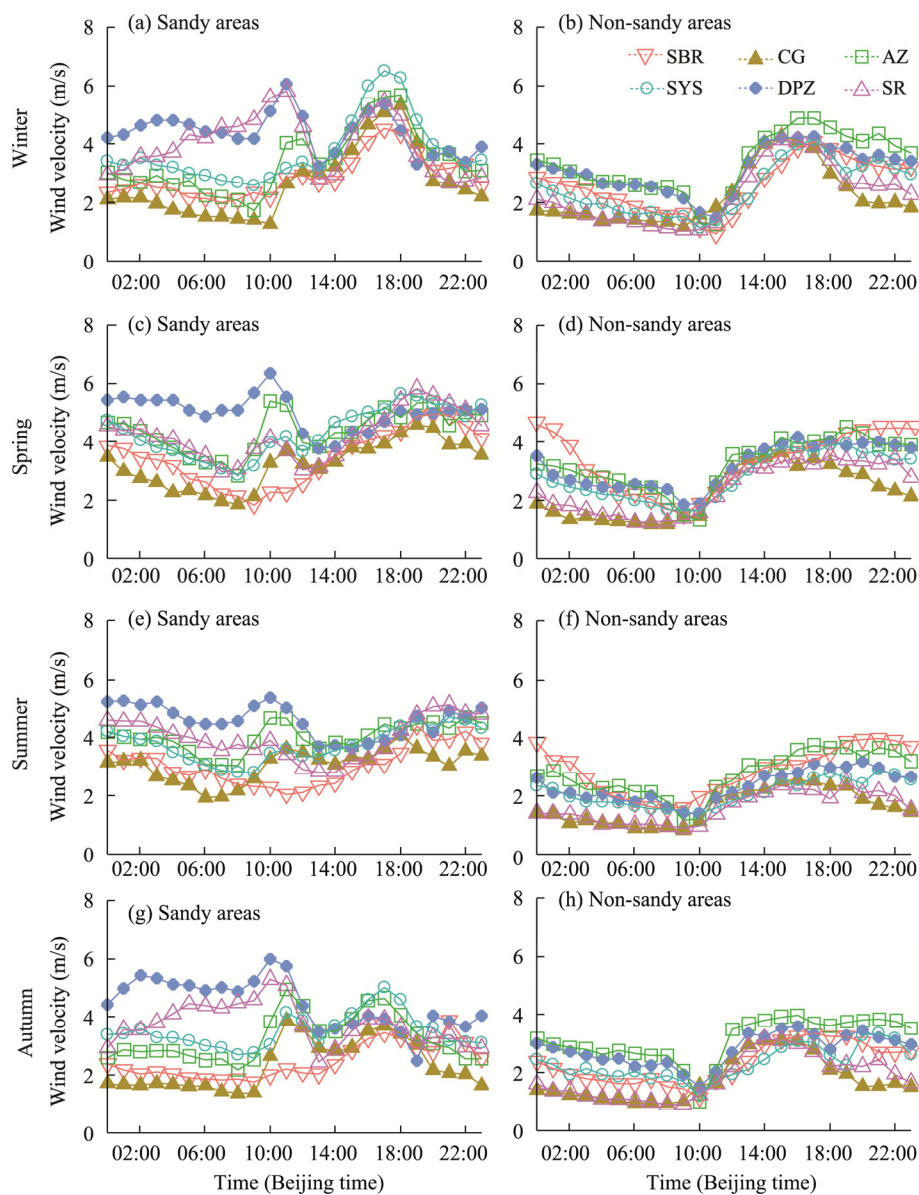


Fig. S3 Diurnal variations of wind velocity in sandy areas and non-sandy areas in winter (a and b), spring (c and d), summer (e and f) and autumn (g and h)